Materials Science & Engineering C 113 (2020) 110962

Contents lists available at ScienceDirect

Materials Science & Engineering C

journal homepage: www.elsevier.com/locate/msec

One-step hydrothermal synthesis with *in situ* milling of biologically relevant hydroxyapatite

Mitchell Chesley[a], Raymond Kennard[a,b], Sahar Roozbahani[a], Su Min Kim[a], Kora Kukk[a], Michael Mason[a,*]

[a] The University of Maine, Department of Chemical and Biomedical Engineering, United States of America
[b] Husson University, Science Department, United States of America

ARTICLE INFO

Keywords:
Biomaterials
Hydroxyapatite
Hydrothermal synthesis
In situ ball milling
Diffuse reflectance

ABSTRACT

Biologically relevant synthetic hydroxyapatite (HA) has become a much-desired material for use within the medical field with an emphasis on orthopedic applications. However, there are very few sources of sub-micron scale HA powders that are economical. Many current procedures to generate synthetic HA, that is both biological and chemically analogous to naturally occurring HA, tend to involve complicated synthesis procedures that are difficult to simultaneously produce desired stoichiometric ratios and particle diameter. This paper reports the development of a one-step hydrothermal method with *in situ* ball milling of synthetic HA. That has the potential to be a biological substitute with similar calcium to phosphate stoichiometric ratio and particle diameter of HA found in many natural biologically occulting sources. Parameters affecting particle diameter investigated included varying ball milling media, *in situ* and *ex situ* ball milling, and simultaneous agitation. The stoichiometric ratios of the resulting powders indicated that 4-hour hydrothermal reaction time produced materials that are analogous to natural HA, confirmed from spectra acquired *via* Fourier Transform Infrared spectroscopy (FT-IR). X-ray diffraction and Scanning Electron Microscopy both indicate that the predominant size of primary crystallites is around ~25 nm. Particle size distributions of dried *in situ* ball-milled HA suggest that primary crystallites exist as aggregates, with aggregate diameters ranging between 1 and 100 μm.

1. Background

1.1. Biological hydroxyapatite

Up to 70% of natural bone is comprised of hydroxyapatite (HA), which includes a number of sub-forms with trace metals and ions such as magnesium, carbonate ions, and acid phosphates, collectively described as bone materials [1,2]. Additionally, natural HA has disordered nanostructures [3] that help to improve bioavailability within applications such as bone implants, with relatively small crystalline domain sizes ~20 nm [2–4] that have been shown to improve the promotion of cell growth [3]. Reportedly, this is in part due to the increased physical interaction between cells and the host material that arises as a result of the large surface-to-volume ratio of the nano-sized particles [5]. Although HA can be extracted from natural sources such as fishbone [6], eggshells [7] and bovine bones [8], these processes can be extremely time consuming and cost-prohibitive.

Synthetic HA (formula of $Ca_5(PO_4)_3OH$), is considered promising bone substitute due to its biocompatibility, osteoconductive and osteoinductive behavior, and ability to create a firm bond with bone tissue [9–13], but typically lacks many of the naturally prevalent ionic substitutions (*e.g.*, F^-, CO_3^{2-}, Na^+, Mg^{2+}, Zn^{2+}, and Sr^{2+}). It has been proposed that synthetic HA material, intended as an implanted scaffolding system, would better promote the *in vivo* growth of mineralized bone with these substitutions [13,14]. Synthetic HA has been created by different methods such as co-precipitation [15], sol-gel [16], hydrothermal processing [17] and solid-state reaction methods [18]. Although these methods are effective in creating materials that are chemically analogous to natural HA, they are generally unable to produce HA materials with the desired submicron particle sizes. As such, a post-synthesis particle milling step is frequently applied to yield micron and nanometer-sized powders. Combined, these mechano-chemical methods can take > 48 h per batch [19]. In general, cost-efficient forms of synthetic HA with sub-micron particle size demonstrating the metabolic activity, dynamic response to the environment, and the immunogenic response of natural HA [4,20] are not yet readily available.

In this study, a simple hydrothermal method presented by Liu et al. [21] was modified to develop an *in situ* one-step synthesis method

* Corresponding author.
E-mail address: michael.mason@maine.edu (M. Mason).

https://doi.org/10.1016/j.msec.2020.110962
Received 19 August 2019; Received in revised form 18 March 2020; Accepted 10 April 2020
Available online 12 April 2020
0928-4931/

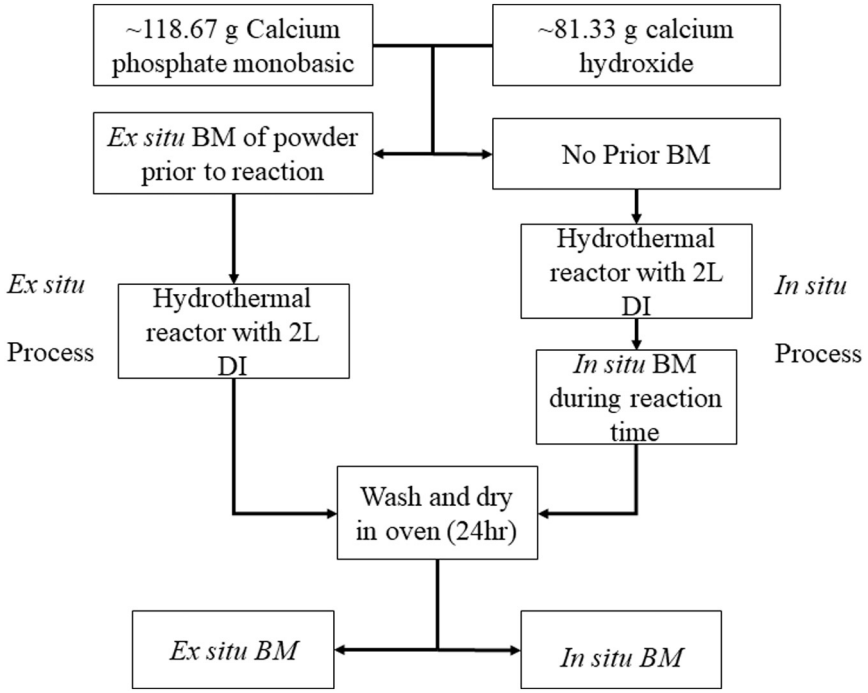

Fig. 1. Process flow diagram for hydrothermal synthesis of HA.

capable of efficiently producing large quantities of biologically relevant HA suitable for use in biological applications and as a precursor for further modification to create chemically and morphologically biomimetic HA. This method presented here explores the use of an *in situ* milling process to create mechanical shearing effects on the HA crystallites during synthesis to reduce and refine the size of final particulates. The simple method also avoids the need for continuous monitoring of pH and temperature that is prevalent in other HA synthesis approaches [15,16,18]. The resulting elemental stoichiometric ratios, and crystallite and aggregate sizes were compared to commercially available, biologically relevant HA. Fourier Transform Infrared spectroscopy (FT-IR) was used to determine the stoichiometric Ca:P ratios in the resulting powders to verify the production of HA, to determine the optimum reaction time, and to confirm that *in situ* and *ex situ* milling did not adversely affect the chemical composition of the synthesized HA. X-ray powder diffraction (XRD) was used to determine the crystallinity and primary crystallite size of the as-prepared samples. A Malvern Mastersizer along with scanning electron microscopy (SEM) and transmission electron microscopy (TEM) were used to characterize particle morphology, including the extent of aggregation and the size distributions of resulting aggregates.

2. Procedure

2.1. Material

Calcium Phosphate, monobasic 90%, pure, and Calcium Hydroxide, 98%, (extra pure) reagents were obtained from Fisher Scientific and used without modification. Reagent grade hydroxyapatite was purchased from Sigma-Aldrich (Product number: 289396) for use as an initial standard for FT-IR measurements. A commercially available electric pressure cooker (Greek Chef, Model: YBE60P), with a temperature controller and manual pressure relief mechanism, was used as a hydrothermal reactor. A 3 lb. capacity ball mill with zirconia milling media (ABmo408, 2 mm diameter) was used to achieve the desired size reduction of both precursors and the final dried *ex situ* HA powders. For use with *in situ* synthesis, a large shaker chest (New Brunswick Scientific CO. Inc., Series 25 Incubator Shaker, Model G-25) was implemented. *In situ* ball milling (BM) was implemented during shaker chest agitation by the addition of 0.5-inch and 1-inch chrome stainless steel ball milling media to the hydrothermal reactor.

2.2. Experimental procedure

A simplified hydrothermal synthesis method for HA developed by Liu et al. [21] was modified for the production of HA in this study. HA was synthesized using a ~200 g total powder mixture, with a 3:7 stoichiometric ratio, of calcium phosphate monobasic to calcium hydroxide, respectively. The mixture was initially placed in the ball mill container along with zirconia milling media, in the ratio of 3:1 milling media to powder, by weight. Samples intended for *ex situ* processing were milled for 1 h to ensure homogeneous mixing before being placed into the hydrothermal reactor with 2 L of DI water. Five different HA samples were synthesized varying the reaction time from 2 to 6 h, in one-hour increments. The temperature was held constant at 109 °C similar to a procedure done by Liu et al. [21], this was done for all reactions. The high pH (> 10) of the resulting concentration of calcium ion of mixture required no other reducing agents for the synthesis of the HA [22]. The resulting solution was left undisturbed for 12 h allow the reactor to cool and for the HA particulates to settle. The as-synthesized precipitated product was then decanted to remove excess water. The remaining material was washed three times with deionized water to ensure the removal of any unreacted precursors. After washing, the product was oven-dried, in air, at 100 °C for 24 h. The resulting powders were bright white in appearance, and clumpy in nature. BM was again implemented, *ex situ*, here to break apart the larger visible clumps, reduce particulate aggregation, and to refine the particle size distribution. Different milling times were explored and the effect on particle size determined. A simplified process flow diagram for the entire synthesis is presented in Fig. 1.

As stoichiometric ratio and (nanoscale) crystalline grain sizes are both critical for biologically relevant HA, synthesis methods that promote homogeneous reactant dispersion are of interest. *In situ* methods involving the use of ultrasonic mixing have previously been implemented and shown to reduce reaction times and promote the production of smaller nano-crystalline particles [23]. This same work,

performed by Poinern et al. [23], suggests that the use of ultrasound can alter the stoichiometric ratio of the product, which may not be desirable. This was mitigated with the use of high thermal post-treatment temperatures (400 °C), which affected nanoparticle shape. In order to avoid these effects, while still producing chemically and morphologically relevant HA, a simple low-cost *in situ* ball-milling method was investigated. This was achieved by securely fastening the hydrothermal reactor system into a fully enclosed Series 25 Incubator Shaker chest, which was operated in an isolated location. The hydrothermal reaction time and shaking frequency were held constant at 4-h and 200 rpm, respectively. With 4 different *in situ* milling variations; no milling media, 1-inch diameter steel milling media only, 0.5-inch diameter steel milling media only, and a ~50:50 mix by weight of 1 and 0.5inch steel milling media. During the synthesis, pressure within the system was held at 50 kPa. Following the reaction, the vessel was allowed to cool to room temperature, safely reducing the internal pressure, as indicated by the external float valve. Residual pressure was relieved using the manual pressure relief valve before opening. The resulting HA samples were oven dried at 100 °C, and coarsely crushed using a ceramic mortar and pestle to break apart large clumps.

2.3. Characterization

Diffuse reflectance Fourier Transform Infrared (FT-IR) was used as a qualitative analysis to confirm the chemical composition of the as-synthesized HA was similar to a reported spectrum of HA by the National Institute of Standards and Technology (NIST). FTIR spectra of each sample were recorded on an FTLA 2000 spectrometer (ABB) using an EasiDrift accessory utilizing a sample to a KBr ratio of 20% w/w *(gain of 1, resolution 4 cm^{-1}, 40 scans per spectrum). All diffuse reflectance spectra were converted to absorbance units using the Kubelka-Munk (K-M) model. The resulting spectra were filtered using a Savitzky-Golay model to reduce the apparent noise fluctuations in the data to ease the comparison of more significant features between samples. For clarity and ease of comparison, the IR spectra background was subtracted (linear), and then normalized to the primary phosphate peak (~1092 cm^{-1}) and separated into two spectroscopic regions of interest.

To facilitate the assessment of the chemical quality and biological relevance of the samples, a traceable, widely accessible HA spectrum was used as a reference and target spectrum throughout this study. This spectrum, reported by (NIST), extracted from synthesized HA, has been shown to be mimetic, with the exception of absent known proteins associated with HA, of naturally occurring bone [24], including Ox femur [25], and fish bone [6]. Relevant spectral features of biological HA should include contributions from phosphate, carbonate, and hydroxyl ions. In contrast, typical high purity reagent grade HA, which is often chosen as a suitable reference, may demonstrate spectral characteristics not representative of HA found in biology. Carbonated substituted HA can be seen within the spectra at peak 1548 cm^{-1} (A-type), 1410 cm^{-1} and 1452 cm^{-1} (B-type). A-type and B-type carbonated HA occurs when the OH^- and PO_4^{-3} in the HA lattice is substituted with CO_3^{-2}, respectively [26].

The resulting as-synthesized HA powder particle size distributions were initially investigated using a Malvern NanoZS dynamic light scattering instrument. However, due to significant sedimentation effects, results were not reliable. As such a Malvern instruments Mastersizer 2000 (Model: APA2000) was used for size analysis of the dried HA. Particle morphology and possible aggregation were investigated by Scanning Electron microscopy (SEM) using both an AMRay 1820 and Zeiss NVision 40 Microscope. SEM micrographs were obtained at 500 μm and 10 μm scale using the AMRay 1820, (10 kV, 40× and 1990×, magnification, respectively). Higher-resolution SEM micrographs (200 nm scale) were acquired at 2 kV (20,160× magnification) using the Zeiss NVision 40. TEM were obtained using a Philips CM10 TEM (180KX).

X-ray diffraction (XRD) was used to assess relative quality as well as identify the crystalline phases present in the as-prepared samples. Diffraction data were obtained using a Panalytical Xpert Pro X-ray Diffractometer, with a parabolic mirror and PIXCEL 255 channel solid-state detector. A 2Θ range of 20–60 was used. Crystalline domain sizes were calculated from the XRD data using the Debye-Scherrer equation and Williamson-Hall equation. Yields were calculated using the mass of fully dried material (120–180 g) compared to the total mass of precursor reagents and were between 60 and 80%. The variation in yield was attributed to inconsistency during the wash steps, where some material loss was likely.

3. Results

3.1. Fourier Transform Infrared spectroscopy

FT-IR spectra for samples synthesized with reaction times of 2–6 h, in one-hour increments, were compared to determine the optimum hydrothermal reaction time. Based on this information 2-hour synthesis times were determined to be inadequate to provide adequate samples, as such size investigation was deemed unnecessary. According to the previous work by Giraldo-Betancur et al. [24], naturally derived HA is chemically distinct from most synthetic forms of HA, having somewhat elevated hydroxyl levels as seen in the OH^- region of Fig. 2. The presence of the relatively weak band at 3570 cm^{-1} can be assigned to the primary absorption of OH^- found within the HA lattice. The strongest absorption bands of phosphate are evident at 1092 cm^{-1} and 1030 cm^{-1}, while the primary absorption bands of carbonate appear at 871 cm^{-1} and 1384 cm^{-1}. Weaker carbonate peaks are also visible at 833 cm^{-1} and 1640 cm^{-1}. The CO_3^{2-} peak is known to result from small amounts of carbonated hydroxyapatite which occurs from PO_4^{3-} reacting with CO_2 in the air [3,17] and is commonly viewed as an impurity in synthetic HA [3,5,23,24]. In fact, up to 8% of HA found in the naturally occurring bone is in this carbonated form, the presence of some carbonate substituted HA is desired [2,11–13,15,27]. The desired OH^- contribution, arising specifically from incorporation in the material lattice that is either entrapped within the HA crystals or sterically hindered, is visible as a narrow but relatively weak peak around 3570 cm^{-1}. Separately, a broad OH^- contribution resulting from adsorbed water, except when aggressive drying or calcination methods are employed, is visible around 3375 cm^{-1}. Using the 3750 cm^{-1} the relative OH^- content can be quantified, for the sole purpose of optimization of a given sample, as the OH^-/PO_4^{3-} ratio (R) as a function of

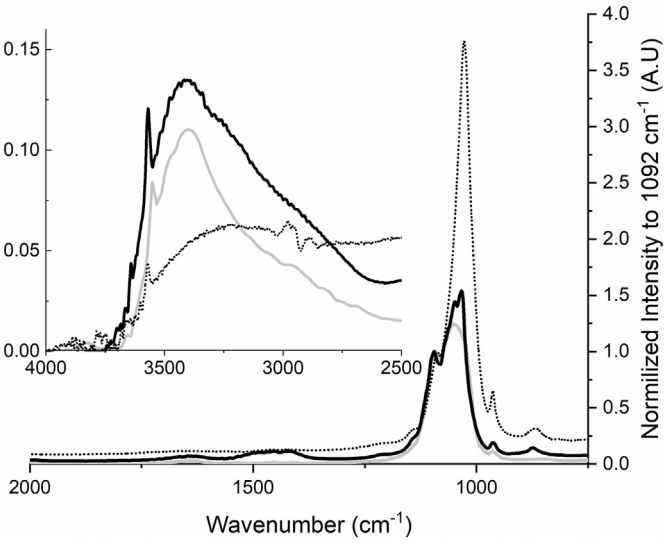

Fig. 2. Spectra of hydroxyapatite from three sources, normalized by the 1092 cm^{-1} phosphate peak following baseline correction. Sigma Aldrich HA (dashed), typical *in situ* 4 h synthesized HA (black), NIST reported HA (grey).

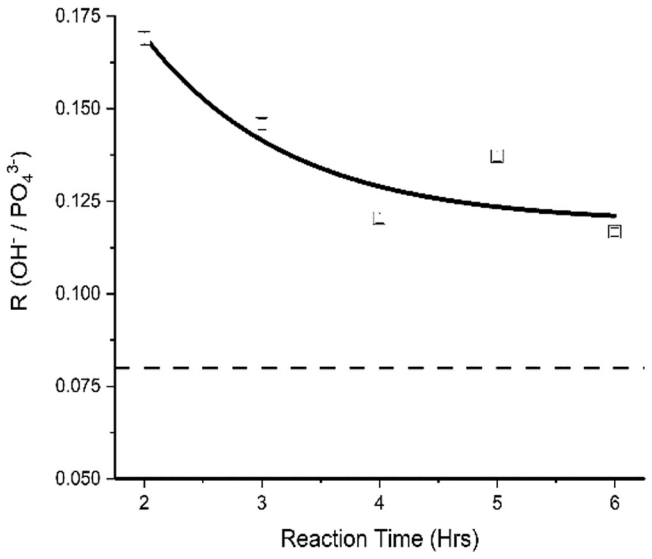

Fig. 3. OH^- relative to PO_4^{3-} peak amplitudes, *vs* reaction time. Target value indicated by dashed line. Experimental values, and corresponding variances, are shown as open squares.

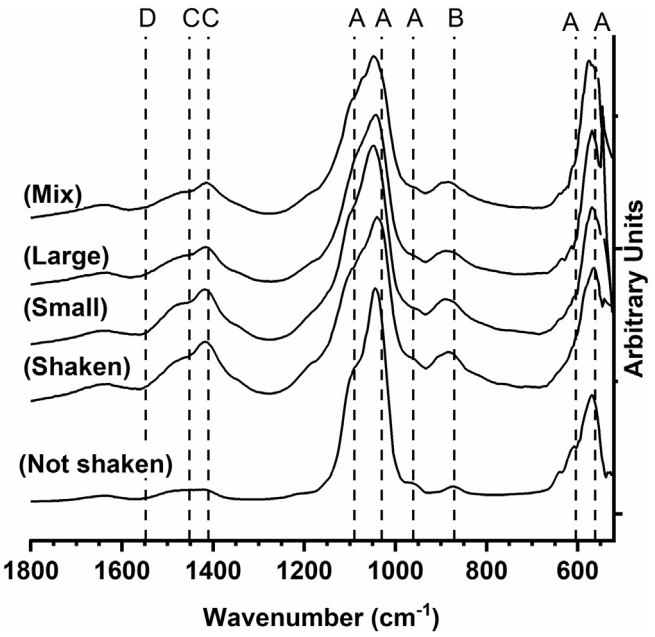

Fig. 4. FTIR spectra of hydroxyapatite synthesized with a reaction time of 4 h. Each of the five samples were prepared under different milling conditions (unmilled, shaken, shaken with *in situ* small media, shaken with *in situ* large media, shaken with *in situ* mixed media). An amplitude offset is used for clarity. A corresponds to PO_4^{3-} (1090, 1030, 602, and 563 cm^{-1}), B corresponds to HPO_4^{2-} (871 cm^{-1}), C corresponds to Type B carbonated HA (1410 and 1452 cm^{-1}), D corresponds to Type A carbonated HA (1548 cm^{-1}).

reaction time. Stoichiometrically, the OH^- content of the material lattice, relative to PO_4^{3-}, for idealized HA should be around 1:3 (R = 0.33) but is expected to be significantly lower when extracted from IR spectra due to the relatively high absorptivity of OH^- relative to PO_4^{3-}. This disparity does not affect the utility of IR spectroscopy in identifying optimal parameters or the value of the NIST spectrum as a target for this optimization.

In order to extract a meaningful value for the OH^-/PO_4^{3-} ratio (R), the IR spectra background was subtracted (linear), and then normalized to primary phosphate peak (~1092 cm^{-1}), which was the only phosphate peak clearly resolved in all spectra. This normalization highlights differences in both the incorporated hydroxyl and phosphate regions of the spectra (Fig. 2). The 3750 cm^{-1} OH^- peak height was measure using the absorbed water peak as a baseline. R values could then be readily determined using the incorporated OH^- peak at 3570 cm^{-1}. A target R-value was determined using the NIST spectrum and is visible as the dashed horizontal line shown in Fig. 3, having an R-value of 0.08. Extracted R-values for all synthesized samples, as a function of hydrothermal reaction time, are shown in Fig. 3. In all cases, the resulting R-values are significantly above that of the target value, with a weak trend indicating that reaction times above 4-hours better approach the target value. Here we note, that the entire R-value exercise was used to identify the most reasonable reaction time, not to quantify the most ideal OH^-/PO_4^{3-} ratio. Based on our results, and for the sake of process efficiency, further studies were performed using a fixed 4-hour hydrothermal reaction time.

To investigate the effects of different milling techniques, and to ensure that the reported novel *in situ* milling technique had no significant effect on the stoichiometric ratio, structural, morphological effects, or contamination from milling media. Several samples using different milling processes were produced and their FT-IR spectra were recorded. Wet and dry milling processes investigated were: *ex situ* dry ball milling, agitation/shaking during synthesis (as a control), shaking with wet *in situ* small steel milling media, shaking with wet *in situ* large steel milling media, and shaking with wet *in situ* mixture of large and small steel milling media. The resulting spectra are shown in Fig. 4. Predominant expected peak positions are indicated as vertical dashed lines for ease of comparison. While minor variations between spectra are visible at the 1050 cm^{-1} band, indicating small structural influences no major differences are observed indicating that the use of milling can be explored to affect particle size without adversely altering the stoichiometric ratio of the HA.

3.2. Particle sizing

3.2.1. Ex situ process

In addition to composition, biologically relevant HA frequently exhibits specific particle and crystalline grain (domain) sizes. As described previously, accessible crystalline grain sizes on the order of a few tens of nanometers are desirable to promote cell growth. Previous work has reported that crystallinity and grain size are affected by reaction conditions. As such, particle size distributions were obtained for each sample, prepared with different hydrothermal reaction times and *ex situ* sample preparations. The resulting volume-weighted size distributions are shown in Fig. 5. To help quantify the effects of reaction time and milling resulting particle size, the size distributions were divided into three regions of interest, the second region (II) corresponding to the targeted size region (10–100 nm diameter). In general, the particle size distributions of the as-synthesized HA samples all exhibited polydispersity with significant volume fractions between 20 μm and 1000 μm, and multimodal with predominant sub-populations centered around 20 μm and 300 μm. It is immediately evident that the 4-h reaction time produces the largest volume fraction of material in the target size region, this is supported by Table 1 which shows the volume percent within different regions. Interestingly, the targeted volume fraction (region II) increases initially with reaction time, then decreases for longer reaction times. This could be a result of continued crystallite growth, agglomeration, or both.

As it is difficult to distinguish between large individual crystallites and aggregates of smaller crystallites using dry particle sizing, a simple mechanical dry milling post-processing step was implemented for each of the as-synthesized samples, in an attempt to break apart aggregates and further increase the volume fraction in the targeted size region. For this, the as-synthesized dried HA (4 h hydrothermal reaction time) was placed in a ceramic rotary milling apparatus with a ratio of 3:1 zirconia ball media to HA powder, by weight. Dry milling was implemented

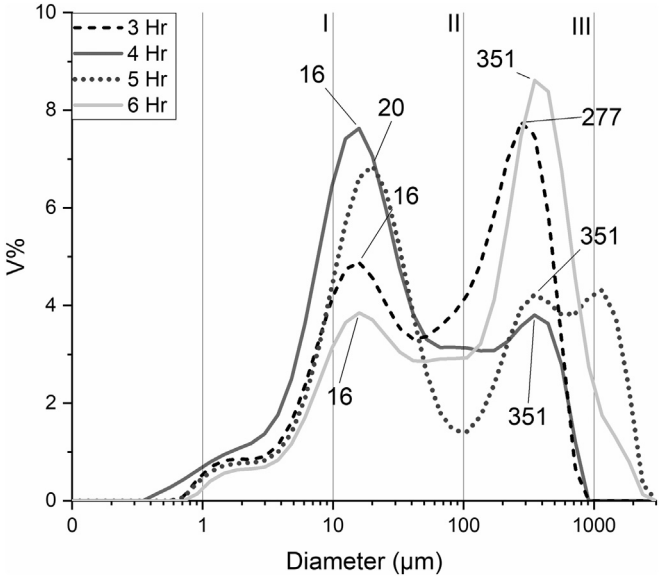

Fig. 5. Size distributions of *ex situ* unmilled HA with different hydrothermal reaction times.

Table 1
Comparison of size distribution, by size region, for HA synthesis times. *Ex situ* process no milling.

Reaction (h)/ Milling (h)	Vol% (± 1%) Region I	Vol% (± 1%) Region II	Vol% (± 1%) Region III	Total Vol% Region I–III
3/0	17	32	47	96
4/0	25	43	28	96
5/0	16	39	29	84
6/0	12	26	51	89

Table 2
Comparison of size distribution, by size region, for HA with different *ex situ* milling times.

Reaction (h)/ Milling (h)	Vol% (± 1%) Region I	Vol% (± 1%) Region II	Vol% (± 1%) Region III	Total Vol% Region I–III
4/0	25	46	28	99
4/1	26	53	19	98
4/4	22	57	19	98
4/24	21	38	30	89

under ambient conditions for durations ranging from 1 to 24 h, after which dry particle size distributions were obtained. The volume fractions for each size region were obtained by integrating the size distribution data. The results are shown in Table 2.

Qualitatively, as the duration of ball milling is increased, the target volume fractions (region I and II) appears to reach a maximum at 4 h. This corresponds to a minimum in the volume fraction of region III. This would seem to suggest that larger particles are either aggregates of smaller particles or are effectively refined by the milling process. This is illustrated in Fig. 6, where the ratio of the volume fractions of region II, relative to region III (R = Vol% II/Vol% III), is plotted as a function of milling duration. At much longer milling times (24 h), this ratio is again reduced, suggesting that aggregation of smaller particles is significant, and may be induced by the milling process itself. This is supported by a similar decrease in the smallest size region (region I) which also shows a decrease in the relative volume fraction with longer milling times.

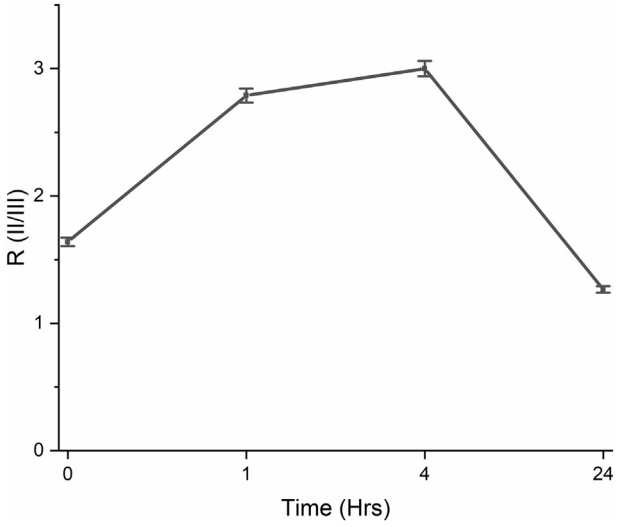

Fig. 6. Comparison of the ratio of volume fractions of region II relative to region III (R = Vol% II/Vol% III), as a function of milling duration.

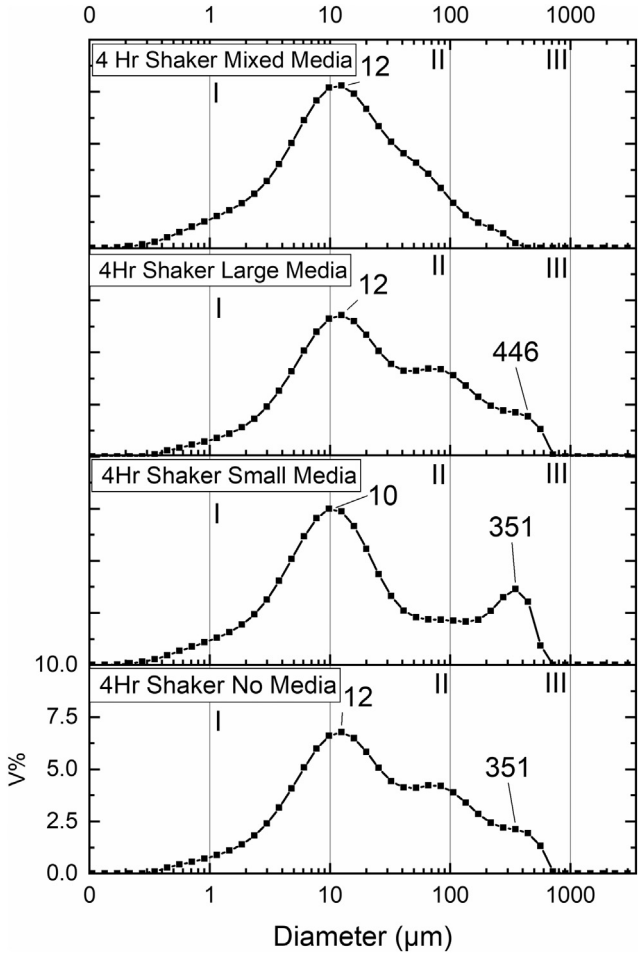

Fig. 7. Particle size distribution for 4 h of hydrothermal treatment with simultaneous shaking, with no ball bearings, *in situ* all large, all small, and 50% small and large milling media, respectively.

3.2.2. *In situ process*

Based on the limited effect of the dry milling experiments on reducing the contribution of the largest volume fraction, an *in situ* wet milling approach was developed based on the work of Kotake et al. [28]. This work compared the effects of dry and wet ball milling,

Table 3
Comparison of size distributions, by size region, for 4 h reaction time with simultaneous shaking and with varying *in situ* milling media.

Milling media	Vol% (± 1%) Region I	Vol% (± 1%) Region II	Vol% (± 1%) Region III	Total Vol% Region I–III
No media	32	45	20	98
Small media	40	36	20	96
Large media	32	45	20	98
Large & small media	41	48	7	96

including the size and shape distribution of the resulting particles. It is perhaps not surprising that this previous work concluding that wet ball milling conditions produced consistently smaller particle sizes. As such a one-step, one-pot hydrothermal synthesis method, which integrates *in situ* mixing and milling of HA, was explored.

In this approach, various sized milling media were introduced directly into the hydrothermal reactor which itself was affixed within a shaker chest providing the necessary periodic motion to achieve mechanical milling simultaneous with mixing (shaking). Due to their hardness and anti-corrosion properties, spherical stainless-steel media were used. The reactor was then affixed within a closed shaker chest to provide simultaneous agitation during a 4h synthesis. Different combinations of milling media sizes were explored, which included: large (1-inch diameter), small (0.5-inch diameter), and equal parts large/small media (by weight). Following hydrothermal treatment/reaction samples were decanted, washed and oven-dried. These samples did not receive additional post-reaction *ex situ* milling, instead, samples were coarsely crushed using a ceramic mortar and pestle to break apart large clumps. The size distributions for these samples are shown for comparison in Fig. 7, while the resulting volume fractions, calculated by integrating across each size region, are presented in Table 3.

The influence of shaking during the 4-r hydrothermal reaction, on the resultant particle sizes is evidenced by the significant decrease in the largest HA size fraction as compared to HA produced in a fixed reactor followed by *ex situ* milling (20% and 28%, respectively). When *in situ* milling is employed simultaneously with shaking, the results are varied. For samples prepared using large milling media, the milling process appears to be largely ineffective, as illustrated by the similarities in the size distributions shown in Fig. 7 and the integrated volume fractions of Table 3. When small milling media is used, the volume fraction of region I is increased, region II is reduced, and region III remains unchanged. Each of these results is consistent with the conventional understanding that larger materials require the use of larger media for effective milling. The largest effect on the size distribution, resulted when equal parts of large and small milling media were used, where the volume fraction of region III decreased by 13%, and both regions I and II increased such that their combined fractions accounted for 89% of the total material volume. In this case, the mixed media may act in a kind of stepwise fashion with the large media first breaking apart the larger particles and aggregates, allowing the smaller media to continue the refining process. While prolonged use of mixed media is generally not recommended as it can result in unwanted wear on the (smaller) media, this was not observed possibly due to the relatively short duration of the milling process employed here.

3.3. Scanning electron microscopy & transition electron microscopy

Scanning electron microscopy (SEM) was used to help elucidate the makeup of the as-produced and milled HA. Specifically, the extent to which the dried as-synthesized HA particles were aggregated, and the varied particle morphologies present were qualitatively investigated. Representative micrographs, across multiple size scales, are shown without modification in Fig. 8 for *ex situ* no BM (A, B, C), and *in situ* milled (mixed media) (D, E, F), HA. The adhesive mounting media used to affix the HA powders is visible as the circular features in the largest area images of Fig. 8(A and D). In these same images, only the aggregates are visible and appear similar in size regardless of whether *ex situ* or *in situ* milling process was used. When viewed at higher magnification (10 μm scale, Fig. 8, B and E respectively), some subtle changes in particle size and morphology start to appear. For example, more of the particles in the *in situ* milled materials (Fig. 8E) appear to be smaller, while there appear to be fewer very large platelets. The *ex situ* particles are also more crystalline in appearance, with large platelets being seen within the image compared to *in situ*. The highest magnification (Fig. 8, C and F), particles with sizes on the order of tens of nanometers are clearly visible in both sample preparations. While there are qualitative differences in morphology and aggregation visible between the two samples, it is difficult to determine if this is sufficiently representative of the entire sample to warrant any significant conclusions.

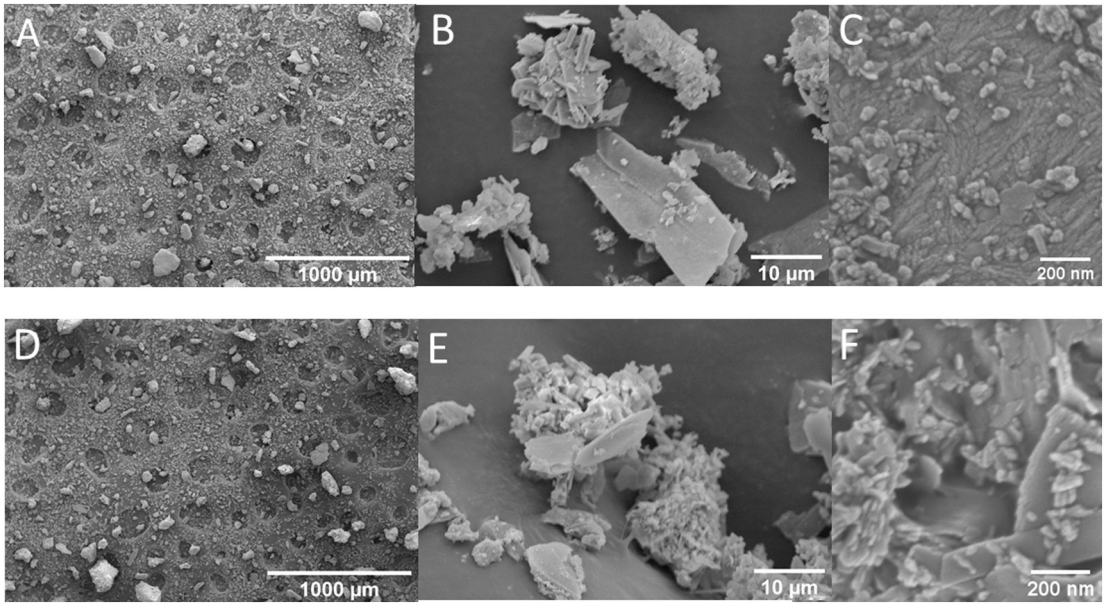

Fig. 8. SEM Images of HA particles with increasing magnification, left to right. A–C) 4 h *ex situ* synthesis, no ball milling. D–F) 4 h *in situ* mixed media.

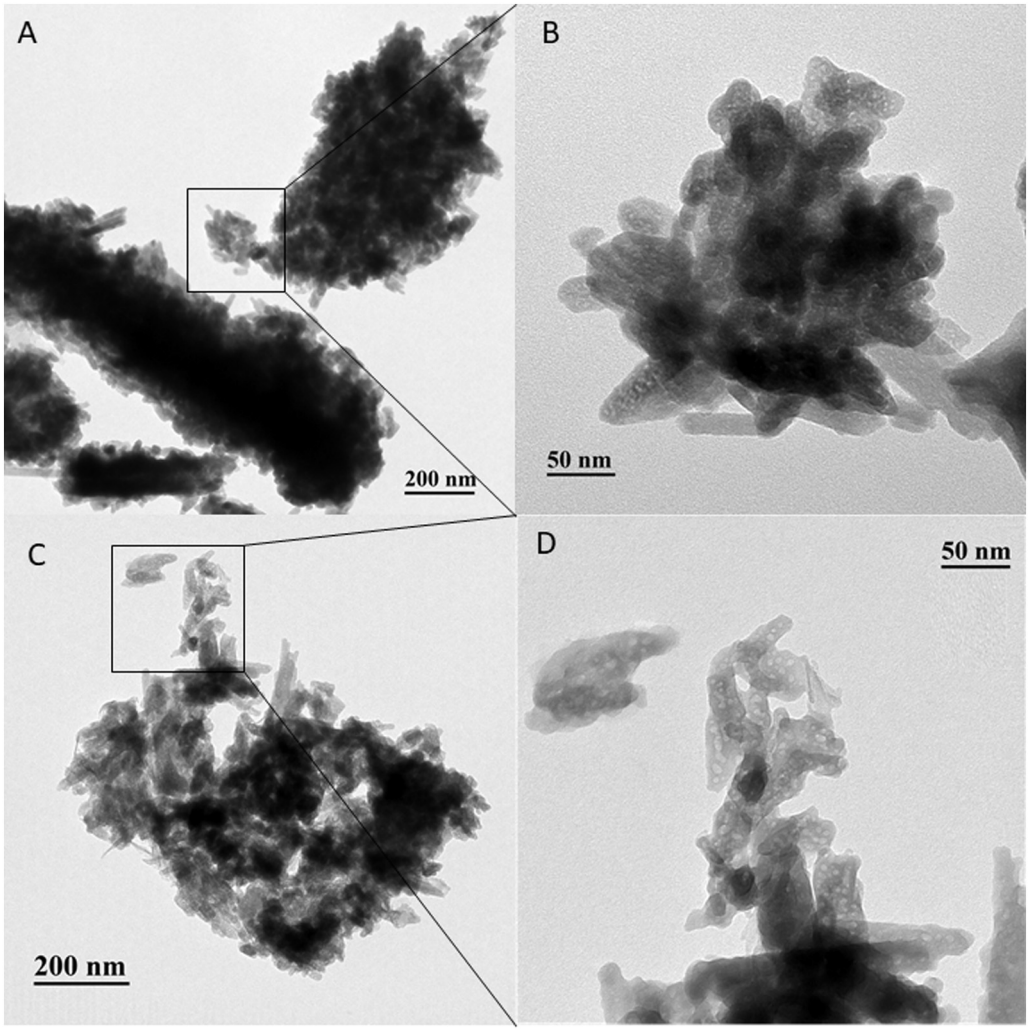

Fig. 9. TEM micrograph of 4-hours *in situ* HA. (A and B No BM, C and D mixed BM).

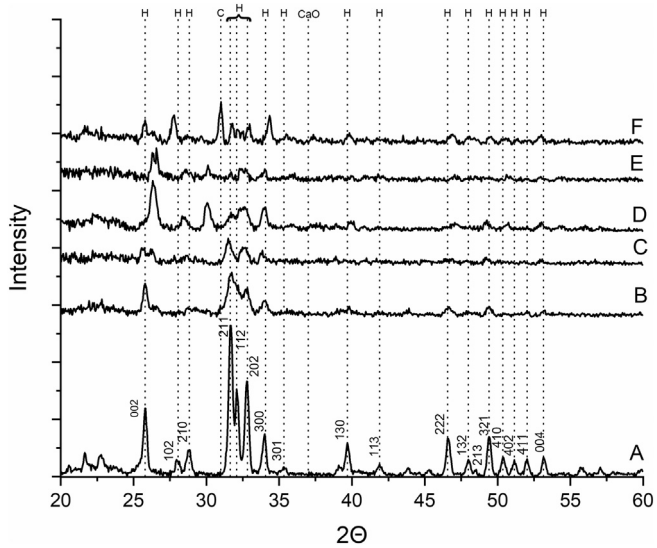

Fig. 10. Comparison of XRD for HA samples. A) Sigma, B) 4 h *ex situ* no BM, C) 24 h *ex situ* milling, D) *in situ* no BM, E) *in situ* mixed media, F) *in situ* mixed media followed by sintering. (H hydroxyapatite, C carbonated hydroxyapatite, CO calcium oxide)

TEM micrograph of 4-h *in situ* shaken HA no BM and mixed BM were taken to as a secondary morphology tool. Samples were sonicated in DI water for ~1 min. TEM images can be seen in Fig. 9, with 4-hour shaken no BM (A & B) and 4-hour shaken mixed BM (C & D). Due to agglomeration and platelets overlaying one another obtaining focus of the agglomerations was difficult as seen in (Fig. 9A & C). With individual particles being seen on the exterior of agglomerates which had better clarity of small platelets. In both images (Fig. 9B & D) individual particulates can be seen around 10–30 nm in diameter, with platelets of agglomerated particles achieving sizes above the 50 nm scale.

3.4. X-ray diffraction

X-ray diffraction data were obtained for all samples in order to qualitatively assess the relative crystallinity of samples as well as estimate the crystalline domain sizes. X-ray diffraction is use here because the dry particle sizing method cannot quantify nanoscale particles near or below the optical diffraction limit or distinguish between nanoparticles and aggregates of nanoparticles. SEM, is similarly limited and cannot differentiate between amorphous and crystalline materials, whereas XRD can determine the size of the crystalline domains of the particles, unobscured by aggregation. Representative XRD data across all synthesized HA sample types is shown in Fig. 10, compared to the commercially available control (Fig. 10A). Here, commonly identified HA peaks are labeled H. The as synthesized HA showed some peak shifting, but were in general agreement with the commonly identified

Table 4
Comparison of calculated HA crystallite size using the Scherrer Eq. (1). As purchased (Sigma) sample is compared to 4 h hydrothermal reactions (4 h) with various reaction and milling conditions.

Sample/Milling conditions	Bragg angle (2Θ Degrees)	ß (FWHM)	Particle size (nm) S (l)	Particle size (nm) WH ($k\lambda/l$)	Strain WH (ε)
Sigma/Unmilled	26	0.3	31	NA	NA
4 h/*Ex situ* unmilled	26	0.3	27	NA	NA
4 h/24 h *ex situ* milled	26	0.3	32	37	0.008
4 h/Shaken *in situ* mixed media	26	0.4	22	36	0.007
4 h/Shaken but unmilled	26	0.4	21	NA	NA
4 h/Shaken, *in situ* mixed media, sintered	26	0.3	28	19	0.001

peaks. Here the primary characteristic HA peaks lie between 25° and 35° and are visible in all samples. Compared to the control, each of the as-synthesized HA samples (B–E) exhibits relatively poor crystallinity as evidenced by the low overall XRD signal. Based on peak intensity, the sample prepared with *in situ* milling (mixed media), Fig. 10E, appears to have the lowest crystallinity. The crystallinity of this material can be somewhat improved by sintering, during which some of the amorphous surface atoms become part of the ordered lattice. This is illustrated in Fig. 10F which shows an apparent increase in the crystallinity of the aforementioned sample, following sintering (3 h, 950 °C) [29]. At Bragg angle 37° there is a small peak corresponding to CaO that has been shown to be caused by the release of carbonated HA during sintering temperatures at 950 °C and higher [30]. A relatively strong peak, labeled as C, appears following sintering, which may be identified as carbonated HA as previously discussed [31].

The predominant size of the particles (or crystalline domain sizes) in each of the HA samples was estimated directly from the XRD data as diffraction analysis is not as susceptible, as the other methods employed here, to the effects of aggregation on the determination. Here the Scherrer (S) Eq. (1) is employed,

$$l = \frac{K * \lambda}{ß * \cos(\Theta)} \quad (1)$$

where K (shape factor) is assumed to be 1, λ is 1.54 Å, ß is the line broadening coefficient, the actual peak width at half the maximum intensity (FWHM) at the Bragg angle, Θ. The selected Bragg angle in each sample is selected to correspond to well resolved and isolated peak positions, optimizing the confidence of the calculations. All Bragg angles as within the primary characteristic HA region. The Scherrer size analysis shows an average crystallite/grain size of 28 nm, across all sample types, with a standard deviation of 5 nm. The results for each sample are shown in Table 4. The largest sizes were for the Sigma, unmilled and 24 h milled HA samples at 31, 27, and 32 nm, respectively. The smallest crystallite sizes were calculated for the shaken samples, with sizes for the *in situ* milled (mixed media) and media-free samples of 22 nm and 21 nm, respectively. For BM samples the Williamson Hall (WH) function (2) was used to estimate size and crystal strain [32]. All variables are the same as Eq. (1) with the addition of ε for

$$\beta * \cos(\theta) = \frac{(k\lambda)}{l} + 2 * \varepsilon * \sin(\theta) \quad (2)$$

strain. With WH, a plot can be created where the Y-intercept is correlated to particle size (l) while the slope is correlated to strain (ε). Due to the poor crystallinity of the as prepared crystals, the diffraction peaks were broad and weak, making precise determination of the FWHM difficult and resulted significant uncertainty in both the particle size and strain determination by the WH equation. The calculated size and strain of the milled specimens are displayed in Table 4. The presence of lattice strain, as a result of milling, is seen by the shifting of maximum diffraction peak angle of 2Θ from an indexed position of 25.79 to 26.23. This has been previously observed by Aminatun et al. [32], where dry ball milling was implemented in the synthesis of HA. The results from these data may suggest that HA crystals formed during synthesis are relatively fragile. It may also indicate that simple agitation through shaking is an effective intermediate step for size reduction.

4. Conclusion

The relatively simple and low-cost single pot method described here was used to produce synthetic but biologically relevant hydroxyapatite (HA) with scalable single batch sizes on the order of 200 g, with typical yields of ~70%. FT-IR spectroscopy of the as-synthesized dried powders confirmed that the as-produced HA exhibited chemical similarity to naturally occurring HA. Traditional post-synthesis *ex situ* (dry) milling methods were compared to an *in situ* (wet) milling approach which was combined with continuous slow agitation by shaking. Dry particle sizing, SEM, TEM, and XRD data all suggest that *in situ* mixed BM is an effective mechanical breakdown technique for HA, reducing dry powder agglomerate size while maintaining particle and individual crystallite sizes around ~22 nm. In addition, it was noticed that *in situ* processing created the addition of A and B type carbonated substituted HA, as seen from FTIR and XRD data, which is beneficial for many biological applications of synthetic HA. Individual BM techniques can induce larger agglomerations of particulates and platelets to form larger dry powder sizes. These HA aggregates may or may not be a concern based on the desired application of the material. Generally, the samples prepared with *in situ* millings appear very similar by SEM, and of at least equivalent quality as the *ex situ* milled sample, mimicking the overall size and stoichiometric ratio of the natural bone mineral. As substitutions of HA have been noted to improve performance within biological systems, the additions of said substitutions within a *in situ* milling process should be investigated in later studies.

Declaration of competing interest

All authors involved with presented manuscript have no conflict of interest to declare.

Acknowledgment

Funding for this project was made possible in part by a grant from the University of Maine System's Research Reinvestment Fund. We would like to thank Justin Crouse at the Advanced Structural and Composite Center for his guidance and assistance.

References

[1] R. November, Engineering of carbonate apatite bone substitute based on composition-transformation of gypsum and calcium hydroxide, Engineering 2010 (May) (2010) 344–352.
[2] B. Clarke, Normal bone anatomy and physiology, Clin. J. Am. Soc. Nephrol. (2008) 131–139.
[3] Z. Geng, et al., Synthesis, characterization, and biological evaluation of nanostructured hydroxyapatite with different dimensions, Nanomaterials 10 (2017) 1–13.
[4] S.M. Zakaria, S. Hussein, S. Zein, M.R. Othman, F. Yang, J.A. Jansen, Nanophase hydroxyapatite as a biomaterial in advanced hard tissue engineering: a review, Tissue Eng. Part B 19 (5) (2013).

[5] M.H. Fathi, A. Hanifi, V. Mortazavi, Preparation and bioactivity evaluation of bone-like hydroxyapatite nanopowder, J. Mater. Process. Technol. 2 (2007) 536–542.
[6] M. Boutinguiza, J. Pou, R. Comesaña, F. Lusquiños, A. De Carlos, B. León, Biological hydroxyapatite obtained from fish bones, Mater. Sci. Eng. C 32 (3) (2012) 478–486.
[7] S. Lee, et al., Comparative study of hydroxyapatite prepared from seashells and eggshells as a bone graft material, Tissue Eng. 11 (2) (2014) 113–120.
[8] G.S. Johnson, M.R. Mucalo, The processing and characterization of animal- derived bone to yield materials with biomedical applications part 1: modifiable porous implants from bovine condyle cancellous bone and characterization of bone materials as a function of processing, J. Mater. Sci. Mater. Med. 1 (2000) 427–441.
[9] L. Tan, X. Yu, P. Wan, K. Yang, Biodegradable materials for bone repairs: a review, J. Mater. Sci. Technol. 29 (6) (2013) 503–513.
[10] J.T.B. Ratnayake, M.L. Gould, A. Shavandi, M. Mucalo, G.J. Dias, Development and characterization of a xenograft material from New Zealand sourced bovine cancellous bone, Soc. Biomater. (2016) 1054–1062.
[11] W.L. Suchanek, P. Shuk, K. Byrappa, R.E. Riman, K.S. Tenhuisen, V.F. Janas, Mechanochemical – hydrothermal synthesis of carbonated apatite powders at room temperature, Biomaterials 23 (2002) 699–710.
[12] M.D. Giles, R. Scuderi, J.M.D. Alfred, J. Tria, Knee Arthroplasty Handbook Techniques in Total Knee and Revision Arthroplasty, (2006).
[13] Z. Tang, X. Li, Y. Tan, H. Fan, The material and biological characteristics of osteoinductive calcium phosphate ceramics, Regen. Biomater. (2018) 43–59 no. September 2017.
[14] Q. Liu, S. Huang, J.P. Matinlinna, Z. Chen, H. Pan, Insight into biological apatite: physiochemical properties and preparation approaches, Biomed. Res. Int. 2013 (2013).
[15] L.B. Kong, J. Ma, F. Boey, Nanosized hydroxyapatite powders derived from co-precipitation process, J. Mater. Sci. 7 (2002) 1131–1134.
[16] M.H. Fathi, A. Hanifi, Evaluation and characterization of nanostructure hydroxyapatite powder prepared by simple sol – gel method, Mater. Lett. 61 (2007) 3978–3983.
[17] M. Sadat-shojai, M. Khorasani, A. Jamshidi, Hydrothermal processing of hydroxyapatite nanoparticles — a Taguchi experimental design approach, J. Cryst. Growth 361 (2012) 73–84.
[18] Y. Jamie, S. Chye, J. Loo, J. Lee, J. Ma, Investigation of the bioactivity and biocompatibility of different glass interfaces with hydroxyapatite, fluorohydroxyapatite and 58S bioactive glass, BioFactors 30 (2007) 205–216.
[19] K.C.B. Yeong, J. Wang, S.C. Ng, Mechanochemical synthesis of nanocrystalline hydroxyapatite from CaO and CaHPO, Biomaterials 22 (2001) 2705–2712.
[20] S.V. Dorozhkin, Calcium orthophosphate-based biocomposites and hybrid biomaterials, J. Mater. Sci. (2009) 2343–2387.
[21] H.S. Liu, et al., Hydroxyapatite synthesized by a simplified hydrothermal method, Ceram. Int. 8842 (95) (1997) 19–25.
[22] X. Chen, N. Birbilis, T.B. Abbott, A simple route towards a hydroxyapatite – Mg (OH) 2 conversion coating for magnesium, Corros. Sci. 53 (2011) 2263–2268.
[23] G.J. Poinern, R. Brundavanam, X.T. Le, S. Djordjevic, M. Prokic, D. Fawcett, Thermal and ultrasonic influence in the formation of nanometer scale hydroxyapatite bio-ceramic, Int. J. Nanomedicine 6 (2011) 2083–2095.
[24] A.L. Giraldo-Betancur, et al., Comparison of physicochemical properties of bio and commercial hydroxyapatite, Curr. Appl. Phys. 13 (7) (2013) 1383–1390.
[25] M.A. Walters, Y.C. Lang, N.C. Blumenthal, R.Z. Legeros, I.L.A. Konsker, A Raman and infrared spectroscopic investigation of biological hydroxyapatite, J. Inorg. Biochem. 200 (1990) 193–200.
[26] N. Bano, S.S. Jikan, H. Basri, S. Adzila, D.M. Zago, XRD and FTIR study of A & B type carbonated hydroxyapatite extracted from bovine bone, AIP Publ. 20100 (February) (2019) 0–6.
[27] A.A. Chaudhry, J.C. Knowles, I. Rehman, J.A. Darr, Rapid hydrothermal flow synthesis and characterization of carbonate- and silicate-substituted calcium phosphates, J. Biomater. Appl. 28 (3) (2012) 448–461.
[28] N. Kotake, M. Kuboki, S. Kiya, Y. Kanda, Influence of dry and wet grinding conditions on fineness and shape of particle size distribution of product in a ball mill, Adv. Powder Technol. 22 (1) (2011) 86–92.
[29] D. Malina, K. Biernat, A. Sobczak-Kupiec, Studies on sintering process of synthetic hydroxyapatite, Acta Biochim. Pol. 60 (4) (2013) 851–855.
[30] S.M.B.J.V. Rau, S.N. Cesaro, Carbonate release from carbonated hydroxyapatite in the wide temperature range, J. Mater. Sci. Mater. Med. (2006) 597–604.
[31] E. Landi, G. Celotti, G. Logroscino, A. Tampieri, Carbonated hydroxyapatite as bone substitute, J. Eur. Ceram. Soc. 23 (2003) 2931–2937.
[32] A. Supardi, Z.I. Nisa, D. Hikmawati, Synthesis of nanohydroxyapatite from cuttlefish bone (Sepia sp.) using milling method, Int. J. Biomater. 2019 (2019).